OXFORD CDE

Journal of Computational Design and Engineering, 2023, **10**, 250–265

DOI: 10.1093/jcde/qwac137
Advance access publication date: 19 December 2022
Research Article

A control technique for hybrid floating offshore wind turbines using oscillating water columns for generated power fluctuation reduction

Payam Aboutalebi *, Fares M'zoughi, Izaskun Garrido and Aitor J. Garrido

Automatic Control Group–ACG, Institute of Research and Development of Processes–IIDP, Department of Automatic Control and Systems Engineering, Faculty of Engineering of Bilbao, University of the Basque Country–UPV/EHU, Po Rafael Moreno no3, 48013, Bilbao, Spain
*Corresponding author. E-mail: payam.aboutalebi@ehu.eus

Abstract

The inherent oscillating dynamics of floating offshore wind turbines (FOWTs) might result in undesirable oscillatory behavior in both the system states and the generated power outputs, leading to unwanted effects on critical, extreme, and fatigue loads, and finally to a premature failure of the facility. Therefore, this kind of system should be capable of lessening such undesired effects. In this article, four oscillating water columns (OWC) have been installed within a FOWT barge-type platform. A novel switching control technique has been developed in order to reduce oscillations of the system created by both wind and wave, as well as the fluctuations in the generated power, by adequately regulating the airflow control valves. While the impact of the coupled wind-wave loads has been considered, a set of representative case studies have been taken into account for a range of regular waves and wind speeds. The study relies on the use of response amplitude operators (RAO) that have been pre-processed and evaluated in order to apply the switching control technique. In this sense, the starting time of the switching for below-rated, rated, and above-rated wind speeds have been calculated using the platform's corresponding pitch RAO. Additionally, the blades' pitch and generator torque have also been regulated by means of a constant torque variable speed controller to capture maximum energy for below-rated wind speed conditions and to match the rated generator power for rated and above-rated wind speed conditions, respectively. In order to peruse the feasibility and performance of the proposed strategy, a comparison has been carried out between the uncontrolled traditional barge-type platform and the controlled OWCs-based barge FOWT. The results demonstrate that the proposed control approach can effectively and successfully decrease both the oscillations in the system's modes and the fluctuations in the generated power.

Keywords: barge-type floating offshore wind turbine, oscillating water columns, load mitigation

1. Introduction

The usage of conventional fossil fuels such as oil, gas, and coal may promote economic expansion; although excessive use of non-renewable sources release a tremendous amount of carbon dioxide into the atmosphere, resulting in the greenhouse effect. Renewable energy systems have been developed in recent years by government-sponsored initiatives, resulting in the expansion of renewable energy industry (Shahbaz *et al.*, 2020). Hence, the installation of floating offshore wind turbines (FOWTs) throughout the entire world has been gradually developing in order to achieve a low-carbon society and enhance the usage of sea spaces (Kosasih *et al.*, 2020).

One of the issues in the offshore wind sector is the oscillations created by waves and winds on the FOWT's states. These oscillations can cause mechanical issues by putting unwanted loads on the blades, rotor shaft, yaw bearing, and tower, reducing aerodynamic performance and tower fatigue life (Haji *et al.*, 2018). They also have negative impacts on electrical efficiency, leading to undesired system operation security and reliability and fluctuating the generated wind power (Fu *et al.*, 2019). Thus, the oscillations must be within an acceptable range to ensure the stability of the system (Lackner, 2013).

Oscillating water columns (OWCs), as one of the most investigated wave energy converters (WECs), may be integrated into the floating platform in order to dampen the oscillations in the hybrid system (Aboutalebi *et al.*, 2021a). Specifically, barge-based FOWTs provide an easier way to the integration of OWCs into the platform, compared to other types of FOWTs. They also can be used to harness energy from incoming waves through the compression and decompression of the trapped air inside the chambers (Falcão & Henriques, 2016). Besides, adding additional WECs to the FOWTs significantly decrease the WEC's steel frame, mooring lines, electric transmission lines, and siting/permitting expenses, which can account for up to 56% of the cost of a freestanding WEC. For ocean stability, a 5 MW FOWT presently needs up to 1700 tons of platform steel and 5700 tons of ballast concrete in spar-type FOWTs (Kluger *et al.*, 2017). If the WEC stabilizes the FOWT, the necessary aforementioned material may be decreased. This hybrid system can be opted to decrease the levelized cost of energy while also improving the quality of power delivered to the grid.

On the other hand, four types of generators can be applied in wind energy generation systems (Singh *et al.*, 2014), including fixed-speed wind turbines, variable-speed wind turbines, doubly fed induction generator (DFIG) wind turbines, and full-converter

Received: June 21, 2022. **Revised:** November 24, 2022. **Accepted:** December 14, 2022

wind turbines. The first type, known as fixed-speed wind turbines or the Danish concept, uses squirrel-cage induction machines (Ganthia *et al.*, 2021). Therefore, these constant-speed machines, connected directly to the grid, cannot contribute to voltage control. The second type, known as variable-speed wind turbines, can operate at a variety of rotor speeds, giving the possibility of power regulation (Song *et al.*, 2020). DFIG turbines, which compose the third type of generator, tackle the issue of power loss in the rotor circuit and keep the amplitude and frequency of the output voltages constant using a back-to-back AC/DC/AC converter in the rotor circuit to recover slip power (Ebrahimkhani, 2016; Shiravani *et al.*, 2022). The last type of generator, called full-converter turbines, employs a back-to-back AC/DC/AC converter as the only power flow path from a wind turbine to the grid. As a result, there is no direct grid connection, and the converter is rated to manage the full output power (Trevisan *et al.*, 2018). The model for the 5 MW wind turbine designed in FAST is a conceptual design, giving the ability to design an active torque control.

In order to harness energy from waves as well as wind, the hybrid FOWT-WECs have been proposed by researchers, e.g., configuration of three rotating-flaps WECs attached on a semi-submersible FOWT (Michailides *et al.*, 2016), a hybrid tension leg platform-type FOWT and three point-absorber WECs (Bachynski & Moan, 2013), and the hybrid model of a spar-type FOWT and a torus-shaped point-absorber (Muliawan *et al.*, 2012) are some examples of applying hybrid FOWT-WECs to improve energy efficiency. Shah *et al.* (2021) classified control methods with the aim of power maximization, power regulation, and load mitigation into blade-pitch-based and mass-spring–damper-based for different FOWTs. Several manuscripts have introduced the modified structure of FOWTs in order to suppress the vibrations in the system. Palraj and Rajamanickam (2020) proposed the use of a gyro-stabilizer installed in the barge of a FOWT to control the vibrations in the system. Yang *et al.* (2019a) placed a tuned mass damper (TMD) inside the barge platform to reduce the system's vibrations. The usage of wing motion stabilizers mounted on the foundation of the spar-type FOWT for the stabilization purpose was introduced by Yang *et al.* (2019b). Wei and Zhao (2020) reduced the barge pitch and roll movements of a floating hydrostatic wind turbine by integrating the benefits of a bidirectional tuned liquid column damper and a TMD installed on the FOWT's barge. Kluger *et al.* (2017) have applied surge-mode internal surge TMD, a heave-type internal TMD and an array of heave-type external WEC in a combined spar-type FOWT in order to improve the stability of the system. Kamarlouei *et al.* (2022) considered a semi-submersible FOWT with a concentric array of WEC mounted on a floating platform to control the pitching motions. However, the introduced approaches have not applied WECs in a barge-based FOWT to control the oscillations in the system in order to increase the system's stabilization.

Only a few manuscripts have applied the hybrid structure of barge-based FOWT-OWCs to address full non-linear equations of motion. For instance, Jonkman (2007) developed a closed square-shaped moonpool positioned in the center of the barge, allowing the inclusion of an OWC inside the wind turbine's tower. However, this combined system does not aim to increase the system's stability. Aboutalebi *et al.* (2021a) evaluated the dynamics of hybrid barge-type FOWT-OWCs in different marine states. In the article, two platforms, including the standard barge and four OWCs-based barge platforms, have been compared in the absence of wind. The introduced prototype has not been evaluated to control the airflow inside the OWCs' chambers in order to decrease the oscillations in the system. M'zoughi *et al.* (2021) designed a linear model of combined two OWCs-based FOWTs. The OWCs are operated using a PID controller in order to increase the FOWT's stabilization using an airflow control technique used to decrease the platform's pitch and tower's fore-aft movement. Aboutalebi *et al.* (2021b) designed a switching control strategy based on response amplitude operators (RAO) to improve the general performance of the four OWCs-based barge platforms in terms of oscillation reduction in the absence of wind.

In this context, the main aim of this research work is to reduce undesired oscillations in the system's states and generator power using OWC modules integrated into the FOWT's platform. In this sense, the supervisory control of the OWCs switches from maximum power point tracking power extraction mode, i.e., the usual control employed in this kind of system, to a protection control mode when required. Thus, the main objective of the OWCs is not to extract the maximum power, but to decrease the aforementioned oscillations and/or modify the vibration mode of the FOWT. This article presents the implementation of three controllers consisting of a novel switching controller for the OWCs' valves, blades pitch adjustment, and generator power controller. The switching control technique based on RAO has been implemented with consideration of different wave frequencies and the impact of the wind loads on the hybrid system. RAOs have been plotted and preprocessed to evaluate the response motions of the floating hybrid structure, obtaining a generic procedure to have an input-output system. In addition, a second controller has been employed for the blade-pitch angle adjustment. This blades' pitch has been manipulated from the steady-state values of the blade-pitch angles. As usual, for below-rated wind speeds, the blade-pitch angles have been maintained at zero to maximize the wind energy harness. In the above-rated wind speed, generator torque is held constant, and blade-pitch angles have been adjusted to maintain the nominal generator power of 5 MW. Finally, a third controller comprising variable-speed operation mode based on the generator torque manipulation has been employed in order to evaluate the performance of the switching control technique over the generator power output in various wind speeds scenarios.

This research work is structured as follows: Section 2 describes the equations of motion for the hybrid model of barge-based FOWT-OWCs. Section 3 explains the problems and challenges due to the platform's oscillations over the mechanical-electrical components and generated power. In this section, the system's RAOs have been analyzed, and the control techniques for the OWCs' valves, pitch angle, and generator torque have been expressed. In Section 4, the control strategies have been examined under different sea states and below-rated, rated, and above-rated wind speeds. Finally, Section 5 presents the conclusions of this study.

2. Model Statement

Among three types of FOWT's platforms, including spar-buoy, semi-submersible, and tension-leg platforms, barge-type FOWTs are considered as an extension of the semi-submersible concept. Barge-type FOWTs have been attracting attention to themselves due to their small draft providing the capability of installations in shallower waters and the possibility of installing OWCs inside the platform to absorb the wave loads and reduce the floater's motion (Chuang *et al.*, 2021).

Figure 1 demonstrates a barge-type FOWT equipped with four OWCs. The system has been designed to withstand hydrodynamic and aerodynamic loads in order to harness both wind and wave energies. Eight catenary mooring lines have been attached to the platform to keep it from drifting. Three translational states of

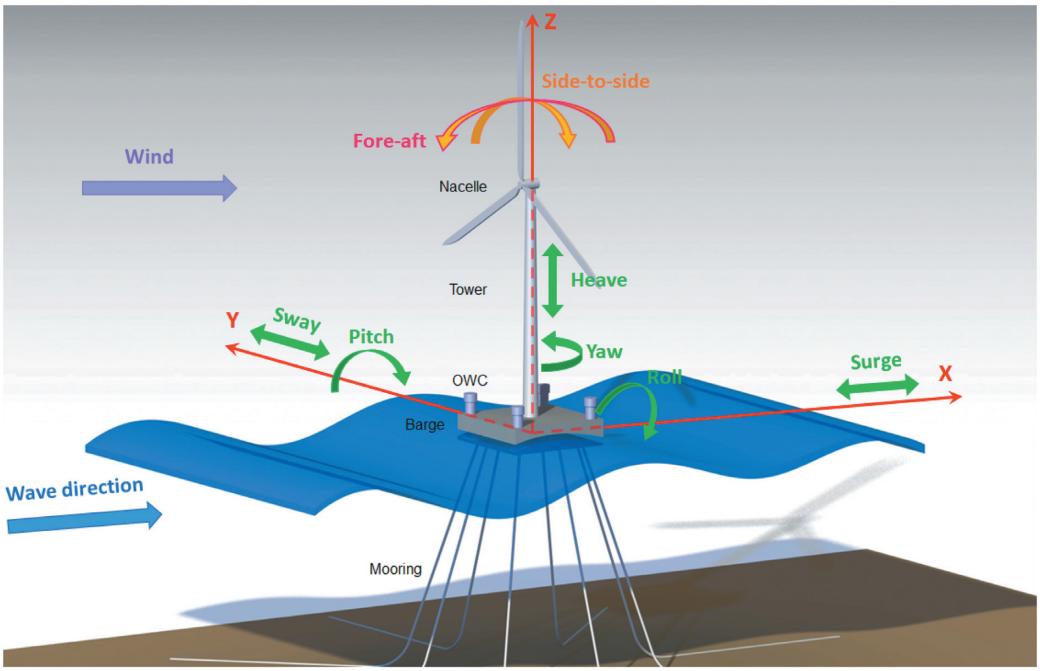

Figure 1: Barge-type FOWT equipped with four OWCs.

Table 1: Concept of FOWT.

Parameter	Value
Hub height	90 m
Center of mass location	38.23 m
Rotor diameter	126 m
Number of blades	3
Initial rotational speed	12.1 rpm
Blades mass	53 220 kg
Nacelle mass	240 000 kg
Hub mass	56 780 kg
Tower mass	347 460 kg
Power output	5 MW
Cut-in, rated, and cut-out wind speed	3, 11.4, and 25 m/s

Table 2: Characteristics of the barge platform with OWCs.

Parameter	Value
Platforms size	40 m × 40 m × 10 m
OWC size	5 m × 5 m × 10 m
Draft and free board for platforms	4 and 6 m
Water displacement for standard barge	6400 m^3
Water displacement for OWCs-based barge	6000 m^3
Mass, including ballast	5 452 000 kg
CM location below SWL	0.281 768 m
Roll inertia about CM	726 900 000 kg m^2
Pitch inertia about CM	726 900 000 kg m^2
Yaw inertia about CM	1453 900 000 kg m^2
Anchor (water) depth	150 m
Separation between opposing anchors	773.8 m
Unstretched line length	473.3 m
Neutral line length resting on seabed	250 m
Line diameter	0.0809 m
Line mass density	130.4 kg/m
Line extensional stiffness	589 000 000 N

the surge, sway, and heave, and three rotational states of the roll, pitch, and yaw have been considered in the FOWT's platform. Also, fore-aft and side-to-side states are in the tower.

The characteristics of the wind turbine and the barge platform with OWCs, respectively, are represented in Tables 1 and 2.

According to airy wave theory, the unidirectional regular waves as an input have been considered that can be described as follows (M'zoughi *et al.*, 2020a):

$$z(t) = A\sin(\omega t) = A\sin(2\pi f t) = A\sin\left(\frac{2\pi}{\lambda}ct\right), \tag{1}$$

where the propagation speed may be defined as $c = \lambda f$ and A expresses the wave amplitude as the distance from still water level (SWL) and the wave crest. λ describes the wavelength as the distance between successive crests and ω denotes the input wave frequency. The wave length can be written as following (Alberdi *et al.*, 2011):

$$\lambda = \frac{gT^2}{2\pi}\tanh\left(\frac{2\pi H}{\lambda}\right), \tag{2}$$

where g is gravitational acceleration and H is wave height. By replacing $T = \frac{2\pi}{\omega}$ in the above equation, the relation between frequency and wave length can be written as follows:

$$\lambda = \frac{2\pi g}{\omega^2}\tanh\left(\frac{2\pi H}{\lambda}\right). \tag{3}$$

Following the expression of surface dynamics, the coupled floating wind turbine, support platform with OWCs have the following non-linear time-domain equations of motion:

$$M_{ij}(x, u, t)\ddot{x}_j = f_i(x, \dot{x}, u, t), \tag{4}$$

where M_{ij} defines the inertia mass elements and x describes the states of the system. u stands for control inputs. The external forces of aerodynamic loads on the blades and nacelle, hydrodynamic forces on the platform, elastic and servo forces, and power

take off (PTO) have been described as f_i on the right hand-side of Equation (4).

The equation of motion in frequency domain can be written as:

$$I_{FOWT}(\omega)\ddot{x} + B_{FOWT}(\omega)\ddot{x} + K_{FOWT}x = \vec{f}_{FOWT}(\omega) + \vec{f}_{PTO}(\omega), \quad (5)$$

where I_{FOWT}, B_{FOWT}, and K_{FOWT} represent the inertia elements, damping components, and stiffness matrix, respectively. $\vec{f}_{FOWT}(\omega)$ denotes the hydrodynamic force, viscous drag, and aerodynamic loads. $\vec{f}_{PTO}(\omega)$ stands for the load caused by the PTO equipment. The term x in Equation (5) is expressed by:

$$x = \begin{bmatrix} \text{surge} \\ \text{sway} \\ \text{heave} \\ \text{roll} \\ \text{pitch} \\ \text{yaw} \\ \text{fore-aft} \\ \text{side-to-side} \end{bmatrix}. \quad (6)$$

The inertia elements of FOWT can be defined by:

$$I_{FOWT}(\omega) = A_{Hydro}(\omega) + M_{Platform} + M_{Tower}, \quad (7)$$

where $M_{Platform}$ is platform mass and M_{Tower} is the tower mass including tower-top rotor-nacelle assembly. The platform mass are described in Appendix 1. A_{Hydro} expresses the platform's added mass, may be calculated by the panel radiation program namely WAMIT.

The stiffness matrix K_{FOWT} may be expressed by:

$$K_{FOWT} = K_{Hydro} + K_{Mooring} + K_{Tower}, \quad (8)$$

where K_{Hydro}, $K_{Mooring}$, and K_{Tower} describe the platform' hydrostatic restoring matrix, the mooring lines spring stiffness elements, and the tower stiffness coefficients, respectively.

The damping coefficients can be described as:

$$B_{FOWT}(\omega) = B_{Hydro}(\omega) + B_{Tower} + B_{viscous} + B_{chamber}, \quad (9)$$

where B_{Hydro} is platform's damping elements from the radiation problem, B_{Tower} is damping matrix of the flexible tower, and $B_{viscous}$ is the viscous drag. $B_{chamber}$ describes the PTO's effect. It is hypothesized that the internal free surface behaves similarly to a piston, resulting in uniform pressure within the chamber (Aubault *et al.*, 2011). As a result, the external force may be defined as following equation:

$$f_{PTO}(\omega) = -p(\omega)S, \quad (10)$$

where the pressure drop throughout the turbine and the internal free surface, respectively, are represented by p and S. Furthermore, it is assumed that air is an ideal gas and the compressed-decompressed air is an isentropic process, so the time-dependent air density can be defined as follows:

$$\rho = \rho_0 \left(\frac{p}{p_0}\right)^{\frac{1}{\gamma}}, \quad (11)$$

where ρ_0 is the density and p_0 is the pressure of the chamber at rest. The heat capacity ratio of air is defined by γ. By linearization of the time derivative of Equation (11), the following equation can be described:

$$\dot{\rho} = \frac{\rho_0}{\gamma p_0}\dot{p}. \quad (12)$$

The linearized mass flow inside of the turbine can be described as follows (M'zoughi *et al.*, 2020b):

$$\dot{m} = \frac{d(\rho V)}{dt} = \frac{\rho_0}{\gamma p_0}\dot{p}V_0 + \rho_0\dot{V}, \quad (13)$$

where V is the air volume into the chamber and V_0 is the air volume in the chamber at rest. A wells turbine with diameter D and rotational velocity N is considered by a linear relationship between the pressure and flow coefficients in non-dimensional turbo-machinery nomenclature as follows:

$$\Psi = K\Phi, \quad (14)$$

where the pressure and flow coefficients, respectively, are defined as follows:

$$\Psi = \frac{p}{\rho_0 N^2 D^2} \quad (15)$$

$$\Phi = \frac{\dot{m}}{\rho_0 N D^3}. \quad (16)$$

Non-dimensionalization is used since the pressure drop is proportional to the flow rate. As a result, the linear relationship, the pressure, and flow coefficients, respectively, can be expressed as follows:

$$\Psi_c = K_c\Phi_c \quad (17)$$

$$\Psi_c = \frac{p}{\rho_0 g H} \quad (18)$$

$$\Phi_c = \frac{2\pi\dot{m}}{\rho_0\omega S H}. \quad (19)$$

The gravitational acceleration is represented by g. As a result of incorporating Equations (17)–(19) into Equation (13), the mass flow inside the turbine can be written as follows:

$$\dot{m}(\omega) = \frac{S\omega p}{2\pi g K_c}. \quad (20)$$

The pressure complex amplitude is expressed by combining Equations (13) and (20):

$$\hat{p}(\omega) = i\omega\frac{\Gamma}{S\omega\left[1+(\varepsilon\Gamma)^2\right]}\hat{V} - \omega^2\frac{\varepsilon\Gamma^2}{S\omega\left[1+(\varepsilon\Gamma)^2\right]}\hat{V}, \quad (21)$$

where $\hat{V}$ is the complex amplitude of the air volume oscillation, and the constants Γ and ε can be written as follows:

$$\Gamma = 2\pi\rho_0 g K_c \quad (22)$$

$$\varepsilon = \frac{V_0}{\gamma p_0 S}. \quad (23)$$

Thus according to Equations (10) and (21), the PTO force can be calculated as follows:

$$\hat{f}_{PTO}(\omega) = -i\omega B_{PTO}\hat{x}_r + \omega^2 K_{PTO}\hat{x}_r, \quad (24)$$

where $\hat{x}_r$ is the relative displacement's complex amplitude. The PTO damping and stiffness elements, respectively, can be defined using Equation (21) as follows:

$$B_{PTO}(\omega) = \frac{\Gamma S}{\omega\left[1+(\varepsilon\Gamma)^2\right]} \quad (25)$$

$$K_{PTO}(\omega) = \frac{\varepsilon\Gamma^2 S}{\omega^2\left[1+(\varepsilon\Gamma)^2\right]}. \quad (26)$$

Thus, the equation of motion in frequency domain for the FOWT is obtained as follows, as described in Equation (5):

$$I_{FOWT}(\omega)\ddot{\hat{x}} + (B_{FOWT}(\omega) + B_{PTO}(\omega))\dot{\hat{x}} + (K_{FOWT} + K_{PTO}(\omega))\hat{x} = \vec{f}_{FOWT}(\omega). \quad (27)$$

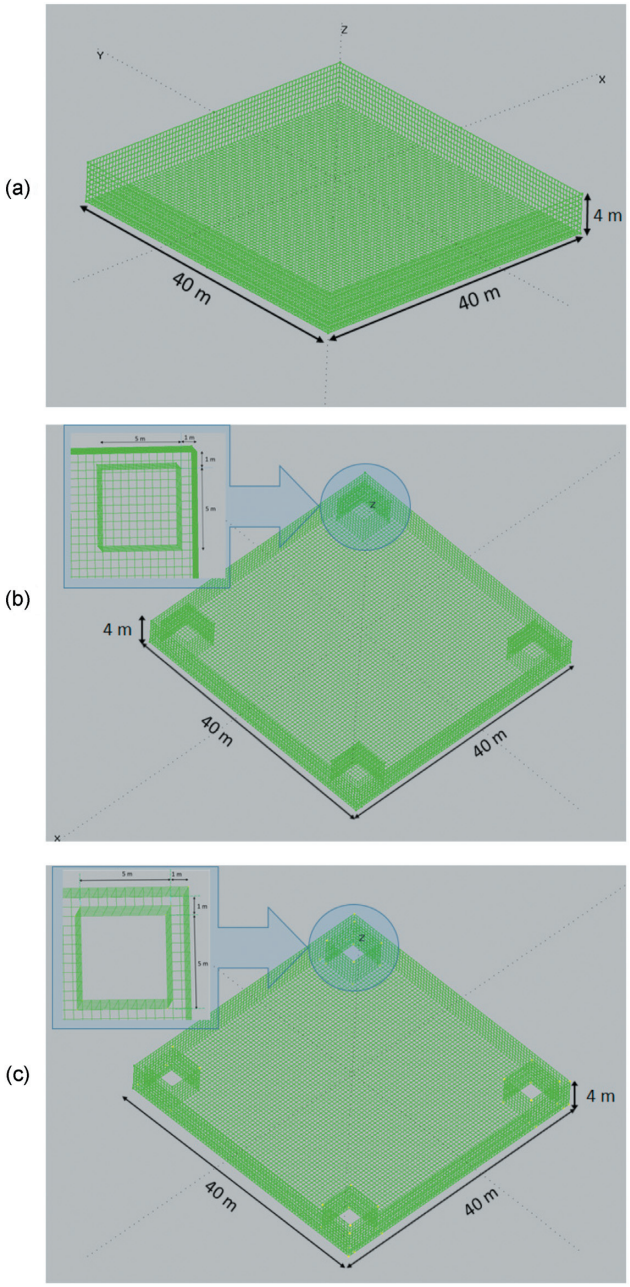

Figure 2: Platforms' design for (a) standard barge platform, (b) closed OWCs-based barge platform, and (c) open OWCs-based barge platform.

In order to define the geometry of the platform, MULTISURF has been used in this research. Figure 2a, b, and c depict three platforms, including the standard barge platform, the closed OWCs-based barge platform, and the open OWCs-based barge platform, respectively. The standard barge platform has been designed with 8960 rectangular panels. The closed OWCs-based barge platform's design has been carried out using 9940 rectangular panels, considering the OWCs' valves are closed. On the other hand, the open OWCs-based barge platform has been meshed using 9840 total rectangular panels, considering the OWCs' valves are open. Note that the platforms' wetted portion has been designed in their undisplaced position so that the considered draft is 4 m.

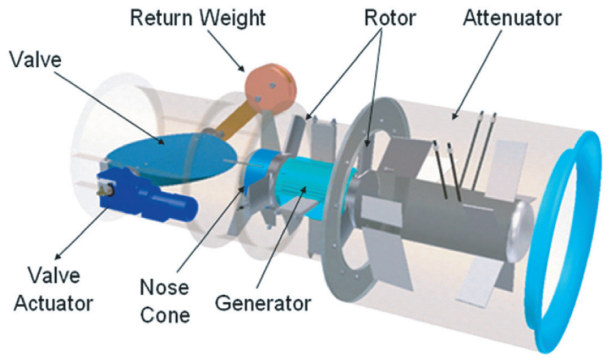

Figure 3: Throttle valve configuration in PTO.

Following the geometry design using MULTISURF, the frequency-dominant matrices of A_{Hydro}, B_{Hydro}, K_{Hydro}, and f_{Hydro} may be calculated using the advanced computational tool, namely WAMIT.

The added mass, damping, and hydrostatic equations are expressed in Appendix 2.

All the simulations results have been obtained using FAST and MATLAB for modeling the barge-based FOWT and control concept for OWCs' valves control, blades' pitch adjustment, and generator torque control for different sea states and wind conditions including bellow-rated, rated, and above-rated wind speeds.

Finally, it should be noted that the OWCs are controlled in order to reduce the platform's oscillations, regardless of the amount of the harvested wave energy, using the chamber's air valve for this purpose. In this sense, each OWC basically consists of an air chamber with a sea opening below the waterline. This chamber is linked to a PTO-based turbine generator. As the waves reach, water is pushed into the chamber, which compresses the air within. The compressed air then operates the turbine, which in turn will provide the torque to the generator. Analogously, the air is pulled out in the opposite direction as the wave water retreats, but the turbine continues rotating in the same direction thanks to its self-rectifying design. Thus, the OWCs have been designed to decrease the oscillations in the system by means of the OWCs' valves which are responsible for the compression/decompression of the air inside the air chambers. Figure 3 illustrates the throttle valve setup in the PTO. A detailed description of the OWC working principle is provided in M'zoughi *et al.* (2018). The rotary valve of the OWCs may provide an adequate air-valve position for each incoming wave, so it responds almost instantaneously to the control signal. The opening and closing time, which may be < 0.3 s (Falcão, 2022), is short enough to respond to the control signals for wave periods > 3 s.

3. Problem Statement

The negative impacts of oscillations in the FOWT's states can cause a variety of problems such as increased maintenance costs, both mechanical due to undesired stress on the system's structures, and electrical due to instability in the generator. These oscillations will also produce a decrement in generated power. To overcome the challenges related to undesired oscillations in the FOWT states, a switching control technique has been introduced. This OWC-based barge platform control decreases the oscillations on the system and reduces the generator power fluctuations.

This section is organized as follows; Section 3.1 covers an introduction to the use of RAOs in floaters. Section 3.2 includes the control statement on the proposed switching control method in

OWCs-based barge platform and the control method for generator power.

3.1. RAOs analysis

The application of RAOs in offshore floaters in order to have an accurate evaluation of the system's behavior is an important evaluation indicator (Ramachandran *et al.*, 2013). RAOs can be plotted and analyzed for the states of the system so that the behavior of the system can be predicted in different environmental conditions (Perez-Collazo *et al.*, 2018).

The frequency-dominant RAOs can be obtained and plotted by employing the tools including MULTISURF, WAMIT, FAST, and MATLAB. MULTISURF creates panels for geometric design in three topologies: standard barge platform, closed OWCs-based barge platform, and open OWCs-based barge platform introduced in the last section. The geometric designs have been used in WAMIT to attain added mass, hydrodynamic, hydrostatic, and damping coefficients. The coefficients are integrated into FAST in order to achieve the system states' RAOs. The RAOs have been achieved where the cross-spectral density of the wave elevation is divided by the auto-spectral density of each system's state, expressed by the following equation:

$$RAO = \frac{S_{xy}(\omega)}{S_{xx}(\omega)}, \tag{28}$$

where $S_{xy}(\omega)$ and $S_{xx}(\omega)$ represent the cross-spectral and auto-spectral densities of the wave elevation input $x(t)$ and the system's states output $y(t)$, respectively. $S_{xy}(\omega)$ and $S_{xx}(\omega)$ are defined as

$$S_{xy}(\omega) = \frac{1}{M}\sum_{s=1}^{M} Y^{[s]}(r)\bar{X}^{[s]}(r) \tag{29}$$

$$S_{xx}(\omega) = \frac{1}{M}\sum_{s=1}^{M} X^{[s]}(r)\bar{X}^{[s]}(r), \tag{30}$$

where $X^{[s]}$ is the fast Fourier transform spectrum of segment s, and M is the number of simulations of the procedure. r is the random noise sequence, and $\bar{X}$ is the complex conjugate of X. Note that M is employed to calculate the average sets for different realizations, leading to a smoother RAO spectrum. In the following RAOs obtaining procedure, an $M = 6$ is considered to appropriately smooth the RAOs spectrum.

In this section, the system states' RAOs with respect to the wave period is presented at three wind speeds, including below-rated wind speed (8 m/s), rated wind speed (11.4 m/s), and above-rated wind speed (18 m/s). The process of RAOs calculation has been for six times ($M = 6$), and wave elevation with a 2 m height in the form of white noise has been considered. Also, both wind and wave directions are aligned with surge mode. For more details on the RAOs calculation process, refer to reference (Aboutalebi *et al.*, 2021b; Pintelon & Schoukens, 2012).

The oscillations in the states of the system for the platforms at three wind conditions can be analyzed in Figs. 4, 5, and 6 at the wind speed of 8, 11.4, and 18 m/s, respectively. In the figures, the green curves, dash-blue curves, and red curves represent the standard barge platform, closed OWCs-based barge platform, and open OWCs-based barge platform, respectively.

Figures 4a, 5a, and 6a illustrate the surge RAOs at those wind speeds. As it is observable, the surge RAOs go up to reach their resonance frequencies for three platforms. From those frequencies, the surge RAOs go down to become stable higher than the surge RAOs 1 m/m. As the RAOs go up or go down, the oscillations in surge increase or decrease, respectively.

Considering the wave and wind directions of zero degrees, the RAOs for sway, side-to-side and yaw are minor, as shown in Figs. 4b,d,g, 5b,d,g, and 6b,d,g. This represents small oscillations in the mentioned states at various environmental conditions.

As seen in Figs. 4e, 5e, and 6e, the roll RAOs arise to reach their natural periods and then, decline to zero. It is observable that there is a shift in the period between the standard barge and/or closed OWCs-based barge platforms and the open OWCs-based barge platform.

The RAOs for the heave state are illustrated in Figs. 4c, 5c, and 6c. It is seen that the heave RAOs arise from shorter wave period to reach the heave RAO 1 m/m in longer wave periods. It means that all platforms follow the wave elevations for long wave periods.

However, platform pitch and fore-aft states are significant because these states are the most provoked modes by the wave and wind with zero directions. The switching control technique is introduced by the pre-processing of pitch RAOs to decrease the oscillations in the system. If the oscillations in platform pitch are decreased, the oscillations in the fore-aft follow the same rule.

It is observed in Figs. 4h, 5h, and 6h that the fore-aft RAOs go up from short-term periods to get to the natural frequencies for all the platforms. Then, the RAOs decrease to get to zero for long-term periods. It means that the platforms do not have oscillations in the fore-aft state for longer periods at all wind speeds.

Oscillations occur in the platform pitch, showed in Figs. 4f, 5f, and 6f for below-rated, rated, and above-rated wind speeds. As the wave period increases, the platform pitch RAOs increase to reach the natural periods. Then, the RAOs decline to get slightly higher than 0 deg/m. The natural periods in the platform pitch for the standard barge platform occur at 11.65, 11.52, and 12.1 s for the wind speeds of 8, 11.4, and 18 m/s, respectively (see Figs. 4f, 5f, and 6f). The natural periods in the platform pitch for the closed OWCs-based barge platform occur as close as the standard barge platform at 11.76, 11.63, and 12.24 s for the wind speeds of 8, 11.4, and 18 m/s, respectively. Moreover, the platform pitch natural periods for the open OWCs-based barge platform are 12.5, 12.4, and 12.96 s, respectively (see Figs. 4f, 5f, and 6f). Hence, based on the platform pitch RAOs, the platform pitch oscillations grow to the natural periods and then decrease to around zero.

3.2. Control statement

In this research work, a switching control technique is introduced in order to reduce the oscillations in the FOWT's states as represented in Fig. 7. The proposed control method is based on the pre-processing of the platform pitch RAOs, illustrated in Figs. 4f, 5f, and 6f at below-rated, rated, and above-rated wind speeds. As it is seen in the figures, the platform pitch RAO for the open OWCs-based barge platform crosses the platform pitch RAOs for the closed OWCs-based platform at a wave period called switching point. These RAOs are used to examine the system behavior when the valves are closed and open for the OWC-based barge platform, which is necessary to analyze and define the switching points. Hence, two different platforms 'standard barge and OWCs-based barge' are mainly used in the paper for comparison purposes. The switching points are the wave periods 12.37, 12.32, and 13.1 s for the wind speeds of 8, 11.4, and 18 m/s, respectively. Therefore, the switching controller opens the valves for the waves with periods lower than the switching points and closes the valves for waves with higher periods than the switching points. It is expected from the platform pitch RAOs that the controlled OWCs-based platform acts almost similar to the standard barge platform for wave periods greater than the switching points while lower oscillations in the platform pitch are expected for the wave periods less than the switching points. The equation for the switching technique is

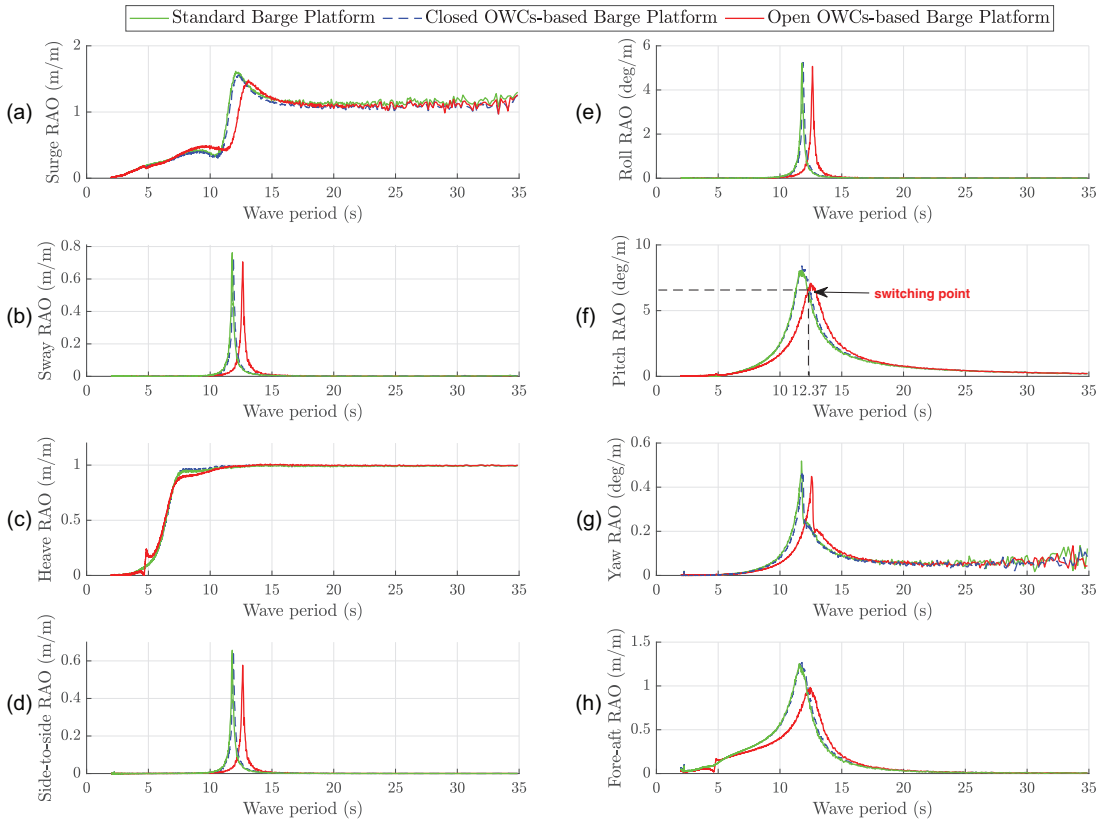

Figure 4: RAOs at the below-rated wind speed of 8 m/s for (a) surge, (b) sway, (c) heave, (d) side-to-side, (e) roll, (f) pitch, (g) yaw, and (h) fore-aft.

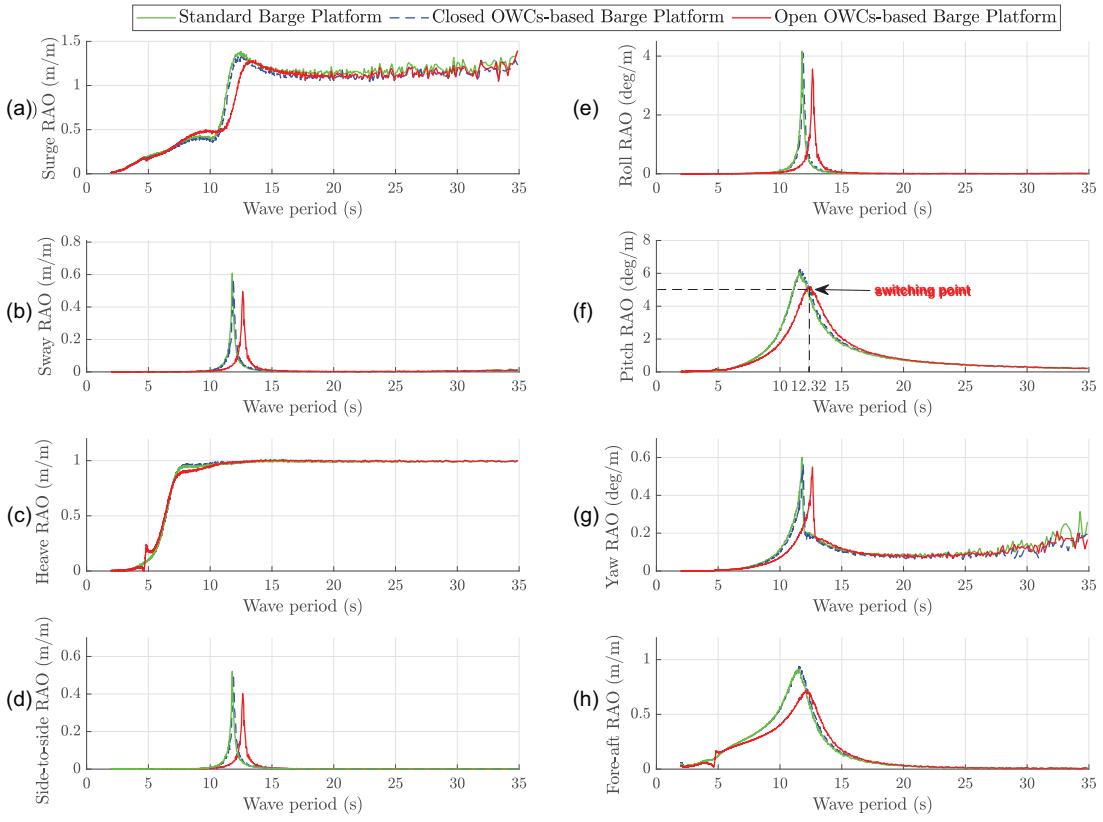

Figure 5: RAOs at the rated wind speed of 11.4 m/s for (a) surge, (b) sway, (c) heave, (d) side-to-side, (e) roll, (f) pitch, (g) yaw, and (h) fore-aft.

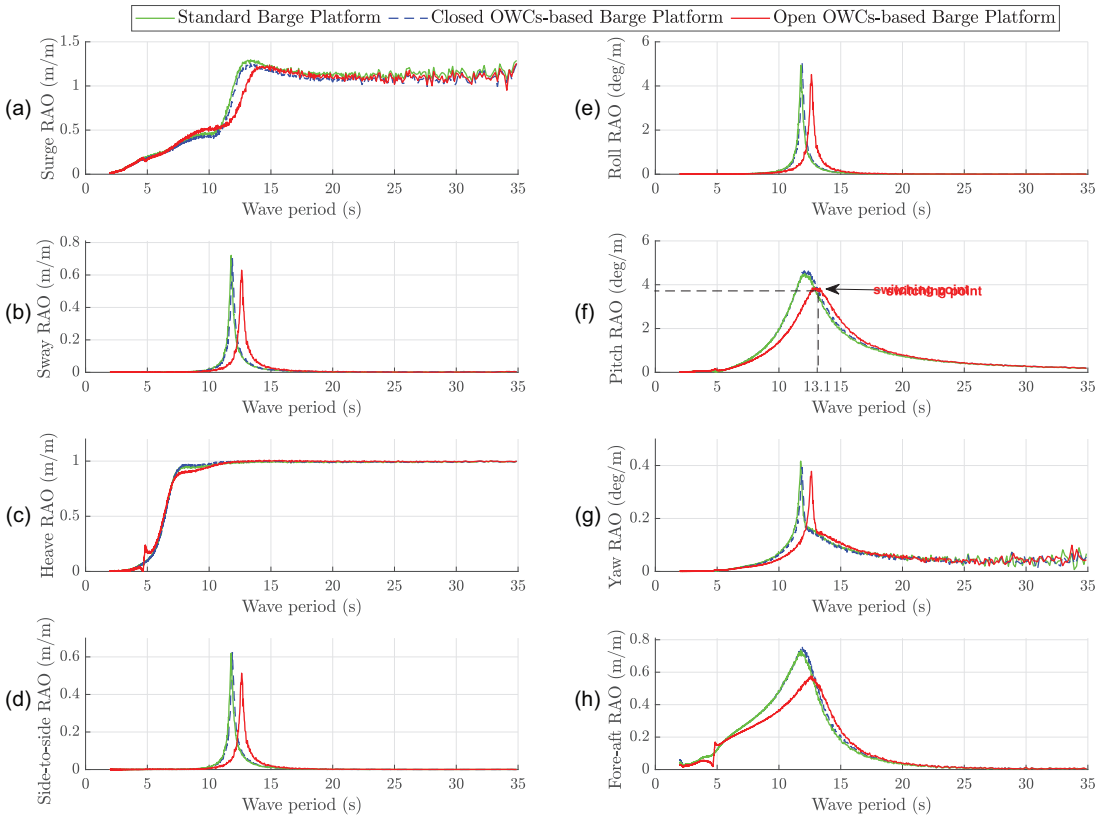

Figure 6: RAOs at the above-rated wind speed of 18 m/s for (a) surge, (b) sway, (c) heave, (d) side-to-side, (e) roll, (f) pitch, (g) yaw, and (h) fore-aft.

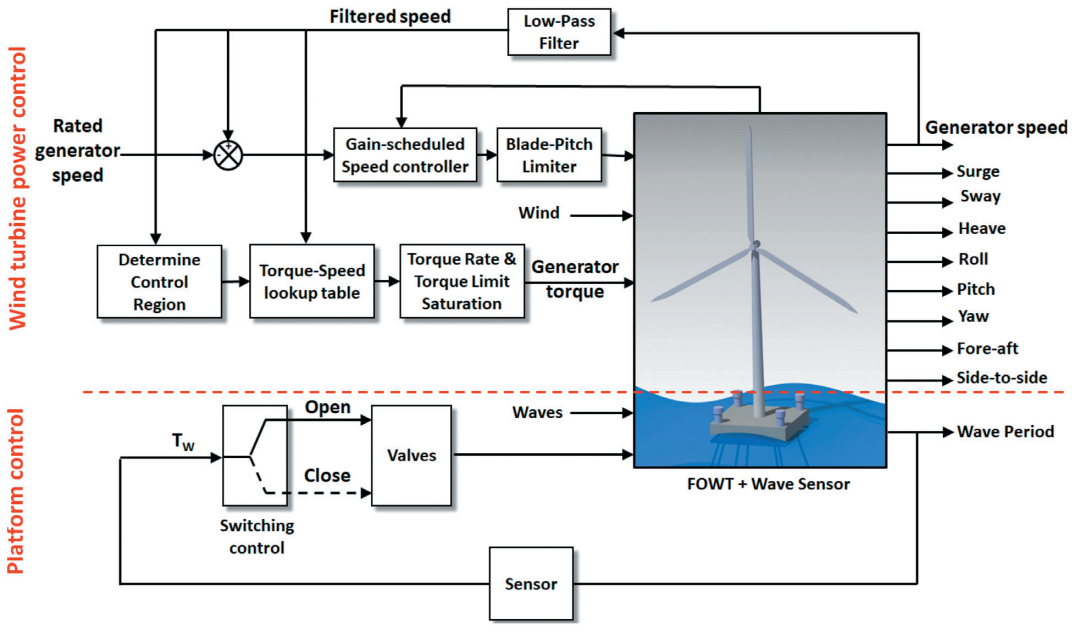

Figure 7: Control scheme for the OWCs-based platform with wind turbine power control at below-rated, rated, and above-rated wind speeds.

defined as follows:

$$u(T_w) = \frac{e^{(T_w - T_{sp})}}{e^{(T_w - T_{sp})} + 1}, \tag{31}$$

where $u(T_w)$ represents a sigmoid function of the closing and opening valves' control input, and T_w expresses the wave period measured by a sensor. Also, T_{sp} is defined as switching point time that depends on the wind speed. The proposed scheme can be considered a semi-active control type since the energy dissipation is ensured by the air valves by modifying the actuator position according to the control signal provided by the controller as a response to the measured wave excitation input continuously measured by the probe sensor.

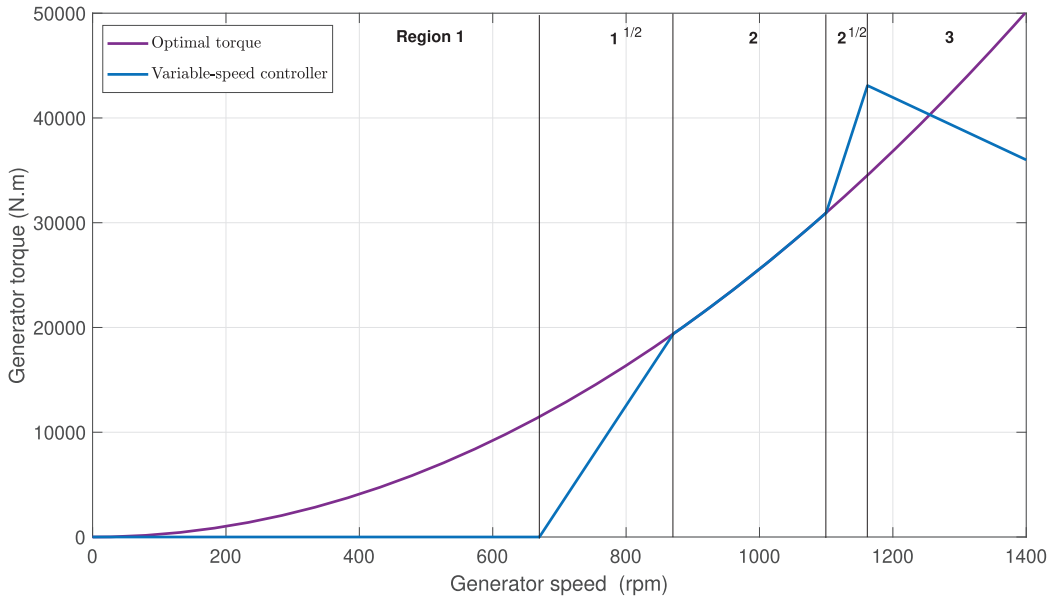

Figure 8: Generator toque versus generator speed.

In the platform control part in Fig. 7, It can be seen that there is feedback from the system exposed to waves. For this purpose, a sensor is attached at the bottom of the OWCs-based barge platform facing the seabed in order to measure the wave periods. Such sensors are called acoustic Doppler current profiler (ADCP). Using the Doppler effect phenomena, they send signals to the seabed and receive them to calculate the wave periods. An ADCP employs a principle of wave sound to measure the wave. When the signals are transferred and received by the ADCP; there is a shift in frequency between the waves called the Doppler shift. By this shift, the ADCP is able to calculate the wave height and direction. Such sensors can measure waves remotely, accurately, and with a high resolution both in time series and depth. They can help increase safety and efficiency, reduce risks, and allow better decision-making in operational situations, which is quite relevant when dealing with offshore platforms. In addition, ADCPs do not have any moving parts, which is a bonus for maintenance and operating in icy waters. These advantages make ADCPs appropriate to be applied in this kind of system. Other types of sensors that can be used to measure sea surface elevation include pressure sensors and buoys.

In this work, a blade-pitch angles adjustment method and variable-speed operation mode based on the generator torque manipulation have been employed in order to evaluate the performance of the switching control technique on the generator power output. The operation regions are divided into five modes, including Regions 1, 1½, 2, 2½, and 3. In Region 1, the wind power is not harvested and the generator torque is zero. In Regions 1½ and 2½, the generator torque is varied in proportion to the generator speed for the linear transition from Region 1 to 2, and from Region 2 to 3, respectively. In Region 2, the generator torque is proportional to the filtered generator speed in order to keep an optimal tip-speed ratio. In Region 3, the generator power is usually kept constant, so that the generator torque results inversely proportional to the filtered generator speed (see Fig. 8). However, a constant torque strategy can also be used for this region. Although each strategy presents its own advantages, this constant torque strategy can be considered more appropriate in the absence of power limitations since the blades' pitch controller can work with less effort to regulate the generator speed, compared to the constant power strategy. The variable-speed control is represented in Fig. 7. For more details on the variable-speed control of the generator, refer to reference (Jonkman, 2007).

Assessment of wind potential has recommended flowing models to harness wind power more efficiently. The following equation for optimal torque for generator torque control in Region 2 respect to speed can be obtained (Hossain, 2018; please see Appendix 3):

$$T_{\text{opt}} = \frac{1}{2}\rho\pi R^5 \frac{C_{p\,\max}}{\lambda_{\text{opt}}^3}\omega^2 = K_{\text{opt}}\omega^2. \tag{32}$$

Considering the 97:1 gearbox ratio, the optimal constant of proportionality in the Region 2 control law is $K_{\text{opt}} = 0.025\,5764$ N m/rpm^2. Regarding the rated generator speed of 1173.7 rpm, rated electric power of 5 MW with a generator efficiency of 94.4%, the rated mechanical power and the rated generator torque are 5.296 610 MW and 43 093.55 N m, respectively. Region 1½ is defined as the range of generator speeds between 670 rpm and 30% above this level equaling 871 rpm. The minimum generator speed of 670 rpm corresponds to the minimum rotor speed of 6.9 rpm for a 5 MW machine. 99% of the rated generator speed (1161.963 rpm) is used as the transitional generator speed between Regions 2½ and 3. A conditional statement on the generator torque controller is added in order to calculate the torque, in Region 3, regardless of generator speed, when the pitch angle is higher or equal to 1 degree. To prevent excessive overloading of the generator and the gearbox, the torque is saturated to a maximum of 10% above rated (47 402.91 N m). A torque rate limit of 15 000 N m/s is also imposed. Figure 8 represents the generator-torque with respect to the generator speed for optimal torque and variable-speed controller in purple and blue, respectively. Note that the variable speed generator torque controller follows the optimal torque only in Region 2.

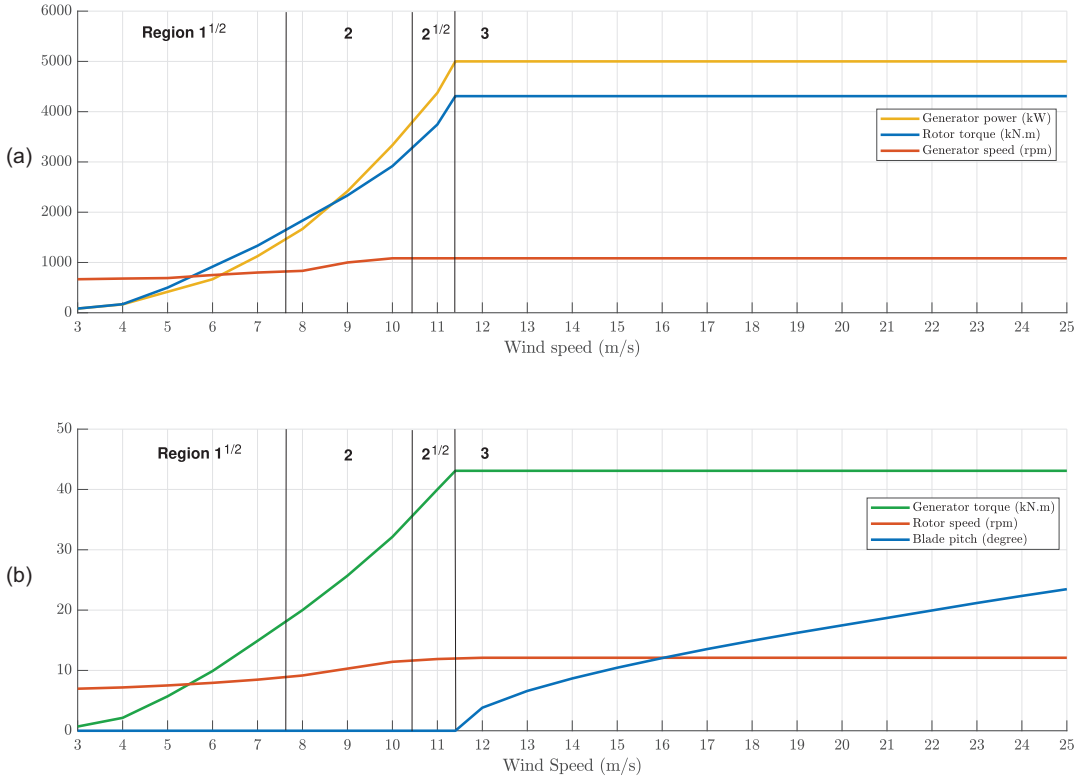

Figure 9: Steady-state values respect with wind speed.

The variable speed generator torque controller implemented in FAST, blue curve, is defined by following expression:

$$T_g(\omega_g) = \begin{cases} 0\ Nm & if\ \omega_g < 670 & \text{Region 1} \\ a_1\,\omega_g + b_1 & if\ 670 \le \omega_g < 871 & \text{Region } 1\frac{1}{2} \\ K_{opt}\omega_g^2 & if\ 871 \le \omega_g < 1160 & \text{Region 2} \\ a_2\,\omega_g + b_2 & if\ 1160 \le \omega_g < 1173.7 & \text{Region } 2\frac{1}{2} \\ a_3 & if\ \omega_g \ge 1173.7 & \text{Region 3} \end{cases}, \quad (33)$$

where $a_1 = 96.53$, $b_1 = -64\,677.68$, $a_2 = 448.68$, $b_2 = -478\,262.97$, and $a_3 = 43\,093.55$ Nm. The generator-torque controller employs the generator speed measurement as the sole feedback input, as is common in utility-scale multi-megawatt wind turbines. A recursive single-pole low-pass filter with exponential smoothing is applied in order to filter the generator speed measurement for the torque controller. It is due to limit high-frequency excitation of the control system. This filter's discrete-time recursion equation is defined as follows:

$$y[n] = (1-\gamma)u[n] + \gamma y[n-1], \quad (34)$$

where $\gamma = e^{-\pi T_s f_c}$, y is the filtered generator speed (output measurement), u is the unfiltered generator speed (input), γ is the low-pass filter coefficient, n is the discrete-time-step counter, T_s is the discrete time step, and f_c is the corner frequency. The filter state is expressed as follows:

$$x[n] = y[n-1] \quad (35)$$

or

$$x[n+1] = y[n]. \quad (36)$$

This filter can be represented in discrete-time state-space as follows:

$$\begin{aligned} x[n+1] &= A_d x[n] + B_d u[n] \\ y[n] &= C_d x[n] + D_d u[n], \end{aligned} \quad (37)$$

where $A_d = \gamma$ and $B_d = 1-\gamma$ are the discrete-time state matrix and the discrete-time input matrix, respectively. $C_d = \gamma$ and $D_d = 1-\gamma$ are the discrete-time output state matrix and the discrete-time input transmission matrix, respectively.

For the blade-pitch angles adjustment, they are manipulated from the steady-state values of the blade-pitch angles as presented in Fig. 9. For below-rated wind speeds, the blade-pitch angles are maintained at zero to maximize energy capture. In above-rated wind speeds, generator torque is held constant and blade-pitch angles are adjusted to maintain the nominal generator power of 5 MW.

4. Results and Discussion

To indicate the performance of the controlled OWCs-based barge platform in comparison with the uncontrolled standard barge platform, a time-domain simulation has been performed. This section covers three scenarios with consideration of both wind and wave for various environmental conditions.

4.1. First scenario

In this scenario, the regular wave with an amplitude of 0.9 m has been considered. The wave period, between 0 and 600 s, is 10 s and then changes to 15 s until 1000 s, as shown in Fig. 10a. The considered constant below-rated wind speed of 8 m/s is aligned with the wave direction of zero degrees. According to the wave and wind directions, and the presented RAOs in Section 3.1, the oscillations in sway, roll, side-to-side, and yaw motions are moderate, whereas surge and heave movements have not been presented because they have negligible impact on generator power output. Hence, the movements of pitch and fore-aft will be studied in order to analyze their impact on generator power, represented in Fig. 10b

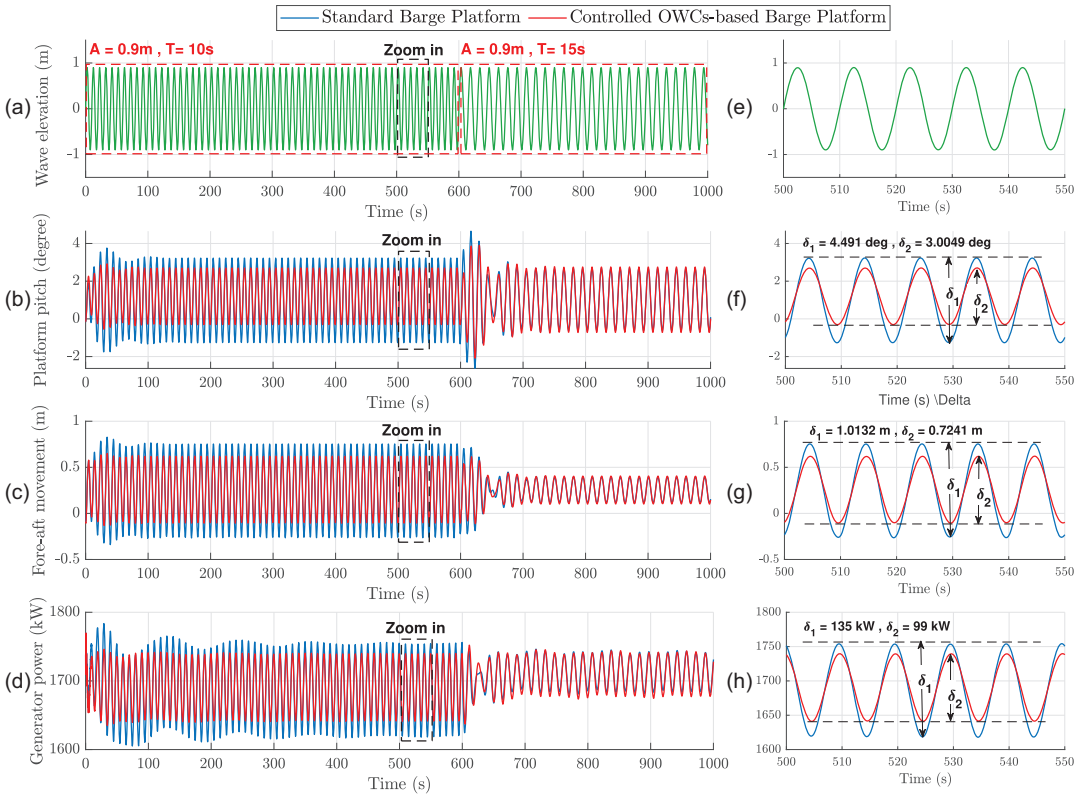

Figure 10: First scenario at below-rated wind speed. (a) Wave elevation. (b) Platform pitch. (c) Fore-aft movement. (d) Generator power.

for platform pitch, Fig. 10c for fore-aft movement, and Fig. 10d for generator power.

Based on the pitch RAO at the wind speed of 8 m/s, the switching controller acts to open the valves for periods 12.37 s and to close the valves for periods > 12.37 s. Here the OWCs' valves transition from the closing to the opening at 600 s.

For comparison purposes, the standard barge platform and the controlled OWCs-based barge platform are represented in blue and red, respectively. As can be seen in Fig. 10b, the controlled OWCs-based barge platform pitches by 3.0049 degrees while the standard barge platform pitches by 4.491 degrees. This illustrates that the pitch oscillations in the controlled OWCs-based platform are drastically lower than the standard barge platform by 33% after transient time. Details can be seen by zooming, as illustrated in Fig. 10f. Both controlled OWCs-based and uncontrolled standard barge platforms' pitch curves are almost identical, with very slight difference after 600 s when the OWCs' controller manages to close the valves.

Fore-aft movement, shown in Fig. 10c, illustrates the same behavior as platform pitch angles for both controlled OWCs-based and standard barge platforms. Before the switching time at 600 s, the controlled OWCs-based barge platform oscillates in fore-aft for 0.7241 m while the standard barge platform' fore-aft oscillates for 1.0132 m. This shows the oscillation deduction by 28.53%. After 600 s, the controlled OWCs-based and standard barge platforms' fore-aft curves are almost identical.

Figure 10d shows the generator power controlled by the variable speed method. In the below-rated wind speed region, the FOWT's blades' pitch moves to zero degrees to extract the most wind energy. It is clearly observed from the figure that there is a relationship between the platform pitch and fore-aft oscillations with generator power fluctuations. Before 600 s, the generator power in controlled OWCs-based barge platform fluctuates to 99 kW, whereas the generator power in the standard barge platform fluctuates to 135 kW. This shows a 26.6% fluctuation reduction in the controlled OWCs-based barge platform, compared with the standard barge platform. Additionally, the average power generators for the controlled OWCs-based and standard barge platform are 1691 and 1686.5 kW, respectively. This illustrates that the controlled OWCs-based platform harvests more wind energy, compared with the standard barge platform.

4.2. Second scenario

The second scenario evaluates the performance of the controlled platform, in comparison with the uncontrolled standard barge platform, under different sea states and the constant rated wind speed of 11.4 m/s. As mentioned in the first scenario discussion, the focus of this article is on the pitch and fore-aft motion. Therefore, the surge, sway, heave, side-to-side, roll, and yaw motions have not been represented. To analyze the switching controller performance in various sea states, two wave periods have been selected, based on the platform pitch RAO, at 10 and 15 s with an amplitude of 1.2 m. The wave period changes from 10 s to 15 s at 600 s, illustrated in Fig. 11a. Both wave and wind directions are aligned with the surge.

The OWCs' controller switches to open the valves for the periods < 12.32 s and to close the valves for the periods > 12.32 s according to the pitch RAO at rated wind speed.

The oscillations in platform pitch before switching at 600 s, shown in Fig. 11b, for the controlled OWCs-based platform is 4.8346 degrees, which is less than the pitch oscillations in the standard barge platform for 6.196 degrees. This represents the less platform pitch oscillation by 21.97% in controlled OWCs-based

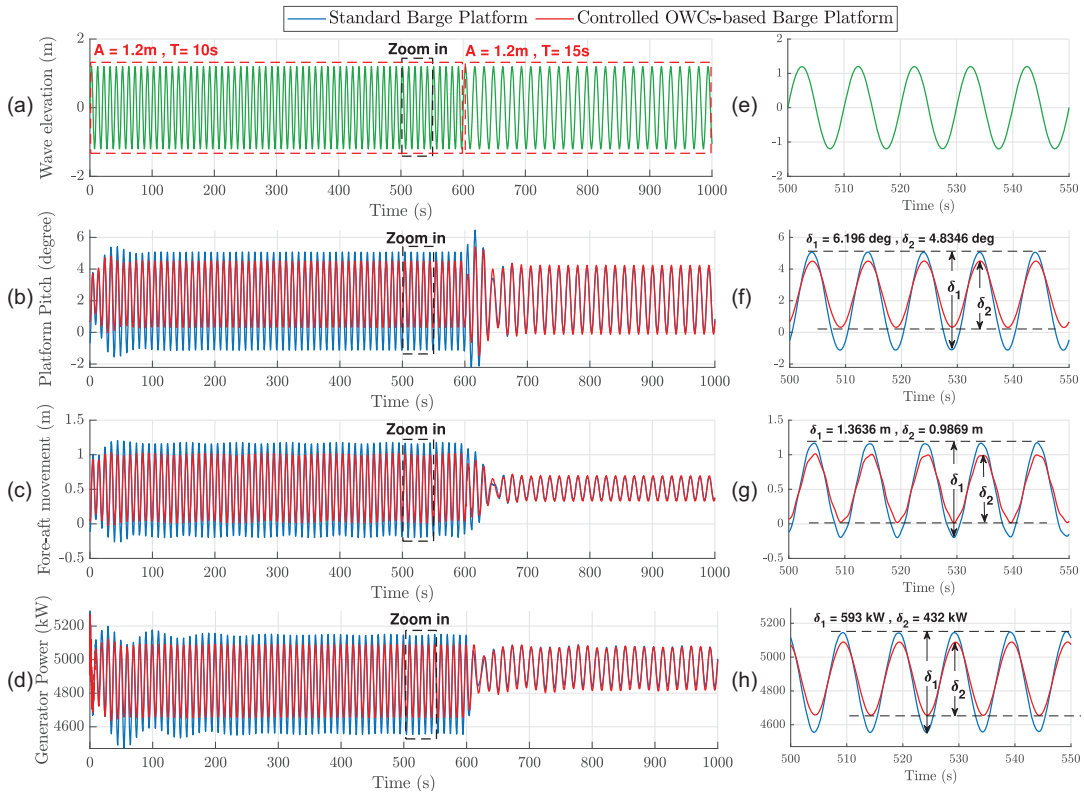

Figure 11: Second scenario at rated wind speed. (a) Wave elevation. (b) Platform pitch. (c) Fore-aft movement. (d) Generator power.

barge platform, compared to the standard barge platform. After 600 s, the switching controller operates to close the valves so that the platform pitch curves for both controlled and uncontrolled platforms are almost identical as expected from pitch RAOs.

Similarly, the same behavior is observable for the fore-aft movement in Fig. 11c. Before switching at 600 s, the fore-aft motion for the controlled OWCs-based barge platform is 0.9869 m while the fore-aft movement for the standard platform is 1.3636 m. It shows a better performance of the controlled OWCs-based barge platform by 27.62%, compared with the standard barge platform. The fore-aft oscillations for both controlled OWCs-based and standard barge platforms are the same after the switching time of 600 s.

The FOWT's blades' pitch is adjusted to zero degrees in order to extract the rated power. The generator power curves for both controlled OWCs-based and standard barge platforms are shown in Fig. 11d. The generator power for the platform with controlled OWCs has less fluctuation before switching at 60 s, in comparison with the standard barge platform. The generator power fluctuations for the controlled OWCs-based and standard barge platforms are 432 and 593 kW, respectively. Hence, the controlled OWCs-based platform has less fluctuation in generator power by 27.15%, compared to the standard barge platform. Moreover, the average generator power for the controlled OWCs-based platform (4871.5 kW) is slightly more than the standard barge platform (4855.5 kW).

4.3. Third scenario

The third scenario has been considered to evaluate the switching controller's performance at the above-rated wind speed and various sea states. The wave and wind directions are set to zero degrees, and the considered wind speed is 18 m/s. Similar to the first and second scenarios, only platform pitch angle, fore-aft movement, and generator power are indicated. The wave elevation with an amplitude of 1.5 m is considered to change at 600 s from wave period 10 to 15 s, as shown in Fig. 12.

As is observed in Fig. 12b, the oscillations in the platform pitch for the controlled OWCs-based barge platform is less than the standard barge platform by 29.90% for the period of 10 s while for the higher period of 15 s, the controlled OWCs-based and standard barge platform represented the same behavior in platform pitch as expected from the platform pitch RAO.

Similar to the platform pitch, the oscillations in fore-aft mode for the controlled OWCs-based barge platform is less than the standard barge platform by 24.50% for the time < 600 s after the transient stage. Both controlled OWCs-based and standard barge platforms have almost the same oscillations in fore-aft state, represented in Fig. 12c.

For the above-rated wind speed of 18 m/s, the blades' pitch are maintained at 14.92 degrees to sustain the rated generator power of 5 MW and the generator torque is kept constant to the nominal generator torque at 43 093.55 N m. Figure 12d illustrates the less fluctuation in generator power for the OWCs-based barge platform, compared to the standard barge platform, by 23.03%. However, after the switching time of 600 s, the controlled OWCs-based and standard barge platforms fluctuate in the generator power almost the same with a slight difference.

Table 3 summarizes all the results for the improvement of the system stability in different weather conditions in three wind speed scenarios and the wave period of 10 s. The table details the oscillations reduction in top tower fore-aft and platform pitch and

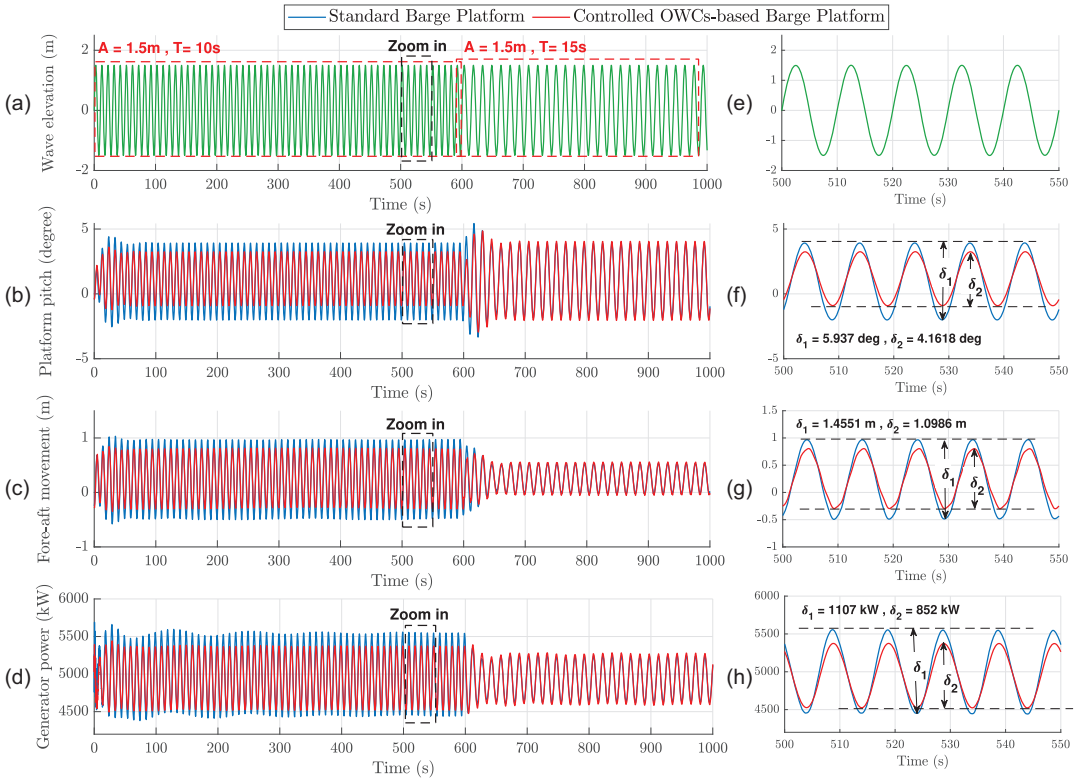

Figure 12: Third scenario at above-rated wind speed. (a) Wave elevation. (b) Platform pitch. (c) Fore-aft movement. (d) Generator power.

Table 3: Oscillations reduction for the proposed controlled platform, compared to standard barge platform.

Scenario	Platform pitch	Top tower fore-aft	Generated power
1. Below-rated wind speed	33.00% reduction	28.53% reduction	26.60% reduction
2. Rated wind speed	21.97% reduction	27.62% reduction	27.15% reduction
3. Above-rated wind speed	29.90% reduction	24.50% reduction	23.03% reduction

fluctuations reduction in generated power for the proposed platform, compared with the standard barge platform.

5. Conclusions

In this research work, different controllers were implemented to mitigate the coupled wind-wave loads. A novel switching control technique was introduced to increase the stability of the FOWT by deduction of the oscillations in the platform and tower modes. The switching controller acts to open and close the OWCs' valves. The system was evaluated in various environmental conditions.

In this article, the wave and wind directions were aligned with the surge mode, and the system was evaluated in various sea states and three wind conditions, including below-rated, rated, and above-rated wind speeds. Hence, all the modes were not provoked, and the focus is on the pitch and fore-aft motions. The transition between opening and closing valves has been conducted by pre-processing the platform pitch RAOs. The platform pitch RAO provides the data for analyzing the behavior of the FOWT. Three platform pitch RAOs for three wind conditions were provided to obtain the switching point time for the OWCs' valves.

From the platform pitch RAOs, the obtained switching points for below-rated, rated, and above-rated wind speeds were the periods of 12.37, 12.32, and 13.1 s. The OWCs' valves switch to the opening and closing states for the periods lower and higher than the mentioned switching points, respectively.

To capture the wind energy, the blades' pitch was adjusted to capture the maximum energy in below-rated wind speed condition and to capture the rated generator power in rated and above rated wind speeds conditions. A variable speed controller for the generator was used to sustain the rated power in Region 3 by constant torque strategy.

The results showed that the proposed switching control technique in OWCs' valves was able to decrease the oscillations in the system effectively for different environmental conditions. The performance of the controlled OWCs-based barge platform in terms of oscillations reduction was better, overall in different environmental conditions, compared to uncontrolled standard barge platform. Moreover, the generator power fluctuations were alleviated efficiently in three considered wind speeds. It was also observed that the average generator power harvested from wind energy in below-rated wind speed for the controlled OWCs-based barge platform was higher than that of the standard barge platform.

The findings of this article will allow further implementation of the proposed method for irregular waves, which are generally

expressed as a combination of modified regular waves. Moreover, the controller's performance in the midst of turbulent wind inflow will be verified.

Acknowledgments

This work was supported in part by the projects PID2021-123543OB-C21 and PID2021-123543OB-C22 (MCIN/AEI /10.13039/501100011033), Basque Government Groups IT1555-22 and Margarita Salas MARSA22/09 (UPV-EHU/MIU/Next Generation, EU).

Conflict of interest statement

None declared.

References

Aboutalebi, P., M'zoughi, F., Garrido, I., & Garrido, A. J. (2021a). Performance analysis on the use of oscillating water column in barge-based floating offshore wind turbines. *Mathematics*, **9**(5), 475. http://dx.doi.org/10.3390/math9050475.

Aboutalebi, P., M'zoughi, F., Martija, I., Garrido, I., & Garrido, A. J. (2021b). Switching control strategy for oscillating water columns based on response amplitude operators for floating offshore wind turbines stabilization. *Applied Sciences*, **11**(11), 5249. http://dx.doi.org/10.3390/app11115249.

Alberdi, M., Amundarain, M., Garrido, A., Garrido, I., Casquero, O., & De la Sen, M. (2011). Complementary control of oscillating water column-based wave energy conversion plants to improve the instantaneous power output. *IEEE Transactions on Energy Conversion*, **26**(4), 1021–1032. http://dx.doi.org/10.1109/TEC.2011.2167332.

Aubault, A., Alves, M., Sarmento, A. N., Roddier, D., & Peiffer, A. (2011). Modeling of an oscillating water column on the floating foundation windfloat. In *Proceedings of the International Conference on Offshore Mechanics and Arctic Engineering*(Vol. **44373**, pp. 235–246). http://dx.doi.org/10.1115/OMAE2011-49014.

Bachynski, E. E., & Moan, T. (2013). Point absorber design for a combined wind and wave energy converter on a tension-leg support structure. In *Proceedings of the International Conference on Offshore Mechanics and Arctic Engineering*(Vol. **55423**, p. V008T09A025). American Society of Mechanical Engineers. http://dx.doi.org/10.1115/OMAE2013-10429.

Chuang, T.-C., Yang, W.-H., & Yang, R.-Y. (2021). Experimental and numerical study of a barge-type FOWT platform under wind and wave load. *Ocean Engineering*, **230**, 109015. http://dx.doi.org/10.1016/j.oceaneng.2021.109015.

Ebrahimkhani, S. (2016). Robust fractional order sliding mode control of doubly-fed induction generator (DFIG)-based wind turbines. *ISA Transactions*, **63**, 343–354. http://dx.doi.org/10.1016/j.isatra.2016.03.003.

Falcão, A. F. (2022). Overview on oscillating water column devices. *Floating Offshore Energy Devices: GREENER*, **20**, 1. http://dx.doi.org/10.21741/9781644901731-1.

Falcão, A. F., & Henriques, J. C. (2016). Oscillating-water-column wave energy converters and air turbines: A review. *Renewable Energy*, **85**, 1391–1424. http://dx.doi.org/10.1016/j.renene.2015.07.086.

Fu, S., Jin, Y., Zheng, Y., & Chamorro, L. P. (2019). Wake and power fluctuations of a model wind turbine subjected to pitch and roll oscillations. *Applied Energy*, **253**, 113605. http://dx.doi.org/10.1016/j.apenergy.2019.113605.

Ganthia, B. P., Barik, S. K., & Nayak, B. (2021). Wind turbines in energy conversion system: Types & techniques. In *Renewable energy and future power systems*(pp. 199–217). Springer. http://dx.doi.org/10.1007/978-981-33-6753-1_9.

Haji, M. N., Kluger, J. M., Sapsis, T. P., & Slocum, A. H. (2018). A symbiotic approach to the design of offshore wind turbines with other energy harvesting systems. *Ocean Engineering*, **169**, 673–681. http://dx.doi.org/10.1016/j.oceaneng.2018.07.026.

Hossain, F. (2018). *Sustainable design and build: Building, energy, roads, bridges, water and sewer systems*. Butterworth-Heinemann. https://books.google.no/books?id=_WFuDwAAQBAJ.

Jonkman, J. M. (2007). *Dynamics modeling and loads analysis of an offshore floating wind turbine*. University of Colorado at Boulder. https://doi.org/10.2172/921803.

Kamarlouei, M., Gaspar, J., Calvario, M., Hallak, T., Mendes, M. J., Thiebaut, F., & Soares, C. G. (2022). Experimental study of wave energy converter arrays adapted to a semi-submersible wind platform. *Renewable Energy*, **188**, 145–163. http://dx.doi.org/10.1016/j.renene.2022.02.014.

Kluger, J. M., Slocum, A. H., & Sapsis, T. P. (2017). A first-order dynamics and cost comparison of wave energy converters combined with floating wind turbines. In *Proceedings of the 27th International Ocean and Polar Engineering Conference*. https://hdl.handle.net/1721.1/123825.

Kosasih, K. M. A., Suzuki, H., Niizato, H., & Okubo, S. (2020). Demonstration experiment and numerical simulation analysis of full-scale barge-type floating offshore wind turbine. *Journal of Marine Science and Engineering*, **8**(11), 880. http://dx.doi.org/10.3390/app10134628.

Lackner, M. A. (2013). An investigation of variable power collective pitch control for load mitigation of floating offshore wind turbines. *Wind energy*, **16**(3), 435–444. http://dx.doi.org/10.1002/we.1502.

Michailides, C., Gao, Z., & Moan, T. (2016). Experimental and numerical study of the response of the offshore combined wind/wave energy concept SFC in extreme environmental conditions. *Marine Structures*, **50**, 35–54. http://dx.doi.org/10.1016/j.marstruc.2016.06.005.

Muliawan, M. J., Karimirad, M., Moan, T., & Gao, Z. (2012). STC (spartorus combination): A combined spar-type floating wind turbine and large point absorber floating wave energy converter' promising and challenging. In *Proceedings of the International Conference on Offshore Mechanics and Arctic Engineering*(Vol. **44946**, pp. 667–676). American Society of Mechanical Engineers.

M'zoughi, F., Aboutalebi, P., Garrido, I., Garrido, A. J., & De La Sen, M. (2021). Complementary airflow control of oscillating water columns for floating offshore wind turbine stabilization. *Mathematics*, **9**(12), 1364. http://dx.doi.org/10.3390/math9121364.

M'zoughi, F., Bouallegue, S., Garrido, A. J., Garrido, I., & Ayadi, M. (2018). Fuzzy gain scheduled PI-based airflow control of an oscillating water column in wave power generation plants. *IEEE Journal of Oceanic Engineering*, **44**(4), 1058–1076. http://dx.doi.org/10.1109/JOE.2018.2848778.

M'zoughi, F., Garrido, I., Garrido, A. J., & De La Sen, M. (2020a). Self-adaptive global-best harmony search algorithm-based airflow control of a wells-turbine-based oscillating-water column. *Applied Sciences*, **10**(13), 4628. http://dx.doi.org/10.3390/app10134628.

M'zoughi, F., Garrido, I., Garrido, A. J., & De La Sen, M. (2020b). ANN-based airflow control for an oscillating water column using surface elevation measurements. *Sensors*, **20**(5), 1352. http://dx.doi.org/10.3390/s20051352.

Palraj, M., & Rajamanickam, P. (2020). Motion control of a barge for offshore wind turbine (OWT) using gyrostabilizer. *Ocean Engineer-*

ing, **209**, 107500. http://dx.doi.org/10.1016/j.oceaneng.2020.107500.

Perez-Collazo, C., Greaves, D., & Iglesias, G. (2018). Hydrodynamic response of the WEC sub-system of a novel hybrid wind-wave energy converter. *Energy Conversion and Management*, **171**, 307–325. http://dx.doi.org/10.1016/j.enconman.2018.05.090.

Pintelon, R., & Schoukens, J. (2012). *System identification: A frequency domain approach*. John Wiley & Sons. http://dx.doi.org/10.1002/9781118287422.

Ramachandran, G., Robertson, A., Jonkman, J., & Masciola, M. D. (2013). Investigation of response amplitude operators for floating offshore wind turbines. In *Proceedings of the 23rd International Offshore and Polar Engineering Conference*. https://www.osti.gov/servlets/purl/1087800.

Shah, K. A., Meng, F., Li, Y., Nagamune, R., Zhou, Y., Ren, Z., & Jiang, Z. (2021). A synthesis of feasible control methods for floating offshore wind turbine system dynamics. *Renewable and Sustainable Energy Reviews*, **151**, 111525. http://dx.doi.org/10.1016/j.rser.2021.111525.

Shahbaz, M., Raghutla, C., Chittedi, K. R., Jiao, Z., & Vo, X. V. (2020). The effect of renewable energy consumption on economic growth: Evidence from the renewable energy country attractive index. *Energy*, **207**, 118162. http://dx.doi.org/10.1016/j.energy.2020.118162.

Shiravani, F., Cortajarena, J. A., Alkorta, P., & Barambones, O. (2022). Generalized predictive control scheme for a wind turbine system. *Sustainability*, **14**(14), 8865. http://dx.doi.org/10.3390/su14148865.

Singh, M., Muljadi, E., Jonkman, J., Gevorgian, V., Girsang, I., & Dhupia, J. (2014). Simulation for wind turbine generators–With FAST and MATLAB-simulink modules. Technical report. National Renewable Energy Laboratory (NREL). https://doi.org/10.2172/1130628.

Song, D., Yang, Y., Zheng, S., Deng, X., Yang, J., Su, M., Tang, W., Yang, X., Huang, L., & Joo, Y. H. (2020). New perspectives on maximum wind energy extraction of variable-speed wind turbines using previewed wind speeds. *Energy Conversion and Management*, **206**, 112496. http://dx.doi.org/10.1016/j.enconman.2020.112496.

Trevisan, A. S., El-Deib, A. A., Gagnon, R., Mahseredjian, J., & Fecteau, M. (2018). Field validated generic EMT-type model of a full converter wind turbine based on a gearless externally excited synchronous generator. *IEEE Transactions on Power Delivery*, **33**(5), 2284–2293. http://dx.doi.org/10.1109/TPWRD.2018.2850848.

Wei, X., & Zhao, X. (2020). Vibration suppression of a floating hydrostatic wind turbine model using bidirectional tuned liquid column mass damper. *Wind Energy*, **23**(10), 1887–1904. http://dx.doi.org/10.1002/we.2524.

Yang, J., He, E., & Hu, Y. (2019a). Dynamic modeling and vibration suppression for an offshore wind turbine with a tuned mass damper in floating platform. *Applied Ocean Research*, **83**, 21–29. http://dx.doi.org/10.1016/j.apor.2018.08.021.

Yang, W., Tian, W., Hvalbye, O., Peng, Z., Wei, K., & Tian, X. (2019b). Experimental research for stabilizing offshore floating wind turbines. *Energies*, **12**(10), 1947. http://dx.doi.org/10.3390/en12101947.

Appendix 1: Platform mass

The platform mass and its diagonal elements are described in Equations (A1–A13) as follows:

$$M_{\text{Platform}} = \begin{bmatrix} m_1 & 0 & 0 & 0 & k_1 & k_2 \\ 0 & m_2 & 0 & k_3 & 0 & k_4 \\ 0 & 0 & m_3 & k_5 & k_6 & 0 \\ 0 & k_3 & k_5 & \beta_1 & k_7 & k_8 \\ k_1 & 0 & k_6 & k_9 & \beta_2 & k_9 \\ k_2 & k_4 & 0 & k_{10} & k_{14} & \beta_3 \end{bmatrix}, \tag{A1}$$

where the elements of the above matrix may be described as follows:

$$\beta_1 = I_{44} + L_Z^2\, m_2 + L_Y^2\, m_3 \tag{A2}$$

$$\beta_2 = I_{55} + L_X^2\, m_3 + L_Z^2\, m_1 \tag{A3}$$

$$\beta_3 = I_{66} + L_Y^2\, m_1 + L_X^2\, m_2 \tag{A4}$$

$$k_1 = L_Z\, m_1 \tag{A5}$$

$$k_2 = -L_Y\, m_1 \tag{A6}$$

$$k_3 = -L_Z\, m_2 \tag{A7}$$

$$k_4 = L_X\, m_2 \tag{A8}$$

$$k_5 = L_Y\, m_3 \tag{A9}$$

$$k_6 = -L_X\, m_3 \tag{A10}$$

$$k_7 = L_X\, L_Y\, m_3 \tag{A11}$$

$$k_8 = -L_X\, L_Z\, m_2 \tag{A12}$$

$$k_9 = -L_Y\, L_Z\, m_1, \tag{A13}$$

where m_1, m_2, and m_3 stand for the inertial mass in translational directions and I_{44}, I_{55}, and I_{66} represent the inertial mass in rotational directions. L_X, L_Y, and L_Z describe the position of the structure's center of mass in SWL coordinates.

Appendix 2: Added mass, damping, and hydrostatic matrices

The added mass and damping elements can be expressed in Equation (B1) and the normalized added mass and damping elements are represented in Equations (B2) and (B3):

$$A_{ij} - \frac{i}{\omega} B_{ij} = \rho \iint_{Sb} n_i \varphi_j \, dS \tag{B1}$$

$$\bar{A}_{ij} = A_{ij}/\rho L^k \tag{B2}$$

$$\bar{B}_{ij} = B_{ij}/\rho L^k \omega, \tag{B3}$$

where L is the length scale, $k = 3$ for $(i, j = 1, 2, 3)$, $k = 4$ for $(i = 1, 2, 3)$, $(j = 4, 5, 6)$ or $(i = 4, 5, 6)$, $(j = 1, 2, 3)$, and $k = 5$ for $(i, j = 4, 5, 6)$.

Due to Gauss' divergence principle, all hydrostatic data can be expressed as surface integrals over the mean body wetted surface S_b so that volume may be defined as follows:

$$\forall = -\iint_{S_b} n_1 x \, dS = -\iint_{S_b} n_2 y \, dS = -\iint_{S_b} n_3 z \, dS. \tag{B4}$$

Hydrostatic elements may be given by:

$$C_{\text{Hydro}} = \begin{bmatrix} 0 & 0 & 0 & 0 & 0 & 0 \\ 0 & 0 & 0 & 0 & 0 & 0 \\ 0 & 0 & c_1 & c_2 & c_3 & 0 \\ 0 & 0 & 0 & c_4 & c_5 & c_6 \\ 0 & 0 & 0 & 0 & c_7 & c_8 \\ 0 & 0 & 0 & 0 & 0 & 0 \end{bmatrix} \tag{B5}$$

and the elements in the above matrix are defined as

$$c_1 = \rho g \iint_{S_b} n_3 \, dS \tag{B6}$$

$$c_2 = \rho g \iint_{S_b} y n_3 dS \tag{B7}$$

$$c_3 = -\rho g \iint_{S_b} x n_3 dS \tag{B8}$$

$$c_4 = \rho g \iint_{S_b} y^2 n_3 dS + \zeta \tag{B9}$$

$$c_5 = -\rho g \iint_{S_b} xy n_3 dS \tag{B10}$$

$$c_6 = \rho g \forall x_b + mgx_g \tag{B11}$$

$$c_7 = \rho g \iint_{S_b} x^2 n_3 dS + \zeta \tag{B12}$$

$$c_8 = -\rho g \forall y_b + mgy_g, \tag{B13}$$

where (x_g, y_g, z_g) are the coordinates of the center of gravity and $\zeta = \rho g \forall z_b - mgz_g$. The coordinates of center of buoyancy may be described as the following equations:

$$x_b = \frac{-1}{2\forall} \iint_{S_b} n_1 x^2 dS \tag{B14}$$

$$y_b = \frac{-1}{2\forall} \iint_{S_b} n_2 y^2 dS \tag{B15}$$

$$z_b = \frac{-1}{2\forall} \iint_{S_b} n_3 z^2 \, dS. \tag{B16}$$

Appendix 3: Standard generator torque control law in Region 2

The critical condition for a wind turbine's mechanical energy is provided by the following equation:

$$P_{MPP} = \frac{1}{2} C_P(\lambda, \beta) \rho A V^3, \tag{C1}$$

where P_{MPP} is the power at the maximum power point, and ρ and C_P express air density (kg/m^3) and power coefficient, respectively. A, V, and λ are defined as the catching range of the rotor area (m^2), the average wind speed (m/s), and the tip speed ratio, respectively. The hypothetical highest estimation of the power coefficient C_p, also known as Betz's coefficient, is 0.593. A wind turbine's tip speed ratio is defined as the ratio of the rotational speed of the blade's tip to the wind speed as defined:

$$\lambda = \frac{R\omega}{V}, \tag{C2}$$

where R, ω, and V are expressed as the range of the turbine (m), the angular speed (rad/s), and the normal wind speed (m/s), respectively. Equation (C2) may be rewritten as

$$V = \frac{R\omega}{\lambda}. \tag{C3}$$

By introducing Equation (C3) to Equation (C1), the power is defined as

$$P = \frac{1}{2} \rho \pi R^5 \frac{\omega^3}{\lambda^3} C_P \tag{C4}$$

while the rotor is rotating at λ_{opt}, $C_p = C_{pmax}$. Hence, Equation (C4) can be rewritten as

$$P = \frac{1}{2} \rho \pi R^5 \frac{C_{p\,max}}{\lambda_{opt}^3} \omega^3 = K_{opt} \omega^3. \tag{C5}$$

It is also possible to describe power as

$$P = \omega T. \tag{C6}$$

Equation (C6) can be recomposed as

$$T = \frac{P}{\omega}. \tag{C7}$$

By Equations (C5) and (C7), the following equation for optimal torque respect to speed can be obtained:

$$T_{opt} = \frac{1}{2} \rho \pi R^5 \frac{C_{p\,max}}{\lambda_{opt}^3} \omega^2 = K_{opt} \omega^2. \tag{C8}$$